MITSUBISHI ELECTRIC RESEARCH LABORATORIES https://www.merl.com

Electric Motor Topology Optimization via Rotated Filter Projection and Adjoint Sensitivities

Das, Ghanendra; Wang, Bingnan; Lin, Chungwei TR2025-164 December 03, 2025

Abstract

We present a unified projection-based framework for topology optimization of electric motor that concurrently handles rotor motion and density filtering on a static finite element mesh. The approach employs a projection operator to map the rotor design onto rotated configurations of the background mesh, thereby eliminating the need for mesh warping, remeshing, or sliding interfaces typically required for simulating rotor motion. The projection further ensures consistent density filtering across all rotation angles. The method's details and implementation are discussed. As a concrete example, we apply this method to a representative synchronous reluctance motor (SynRM) rotor topology optimization problem. A multi-stage optimization strategy is used to handle the nonlinear constraints, resulting in an efficient high-torque rotor design with maximum torque deviation within 1% of the average torque. The results highlight the effectiveness and computational scalability of the proposed framework for high-fidelity electric motor topology optimization.

IEEE Transactions on Magnetics 2025

^{© 2025} IEEE. Personal use of this material is permitted. Permission from IEEE must be obtained for all other uses, in any current or future media, including reprinting/republishing this material for advertising or promotional purposes, creating new collective works, for resale or redistribution to servers or lists, or reuse of any copyrighted component of this work in other works.

Electric Motor Topology Optimization via Rotated Filter Projection and Adjoint Sensitivities

Ghanendra K. Das^{1 2}, Bingnan Wang¹, and Chungwei Lin¹

¹Mitsubishi Electric Research Laboratories, Cambridge, MA 02139,USA, {bwang|clin}@merl.com
²Georgia Institute of Technology, Atlanta, GA, 30332 USA, gdas31@gatech.edu

We present a unified projection-based framework for topology optimization of electric motor that concurrently handles rotor motion and density filtering on a static finite element mesh. The approach employs a projection operator to map the rotor design onto rotated configurations of the background mesh, thereby eliminating the need for mesh warping, remeshing, or sliding interfaces typically required for simulating rotor motion. The projection further ensures consistent density filtering across all rotation angles. The method's details and implementation are discussed. As a concrete example, we apply this method to a representative synchronous reluctance motor (SynRM) rotor topology optimization problem. A multi-stage optimization strategy is used to handle the nonlinear constraints, resulting in an efficient high-torque rotor design with maximum torque deviation within 1% of the average torque. The results highlight the effectiveness and computational scalability of the proposed framework for high-fidelity electric motor topology optimization.

Index Terms—Topology Optimization, Finite Element Analysis, Synchronous Reluctance Motor, Computational Electromagnetics

I. Introduction

TYPICAL design objective of synchronous reluctance motors (SynRM) focuses on maximizing the average torque while minimizing the corresponding ripple [1], [2]. Topology optimization, which explores the design space for optimal material layouts, has been increasingly applied to the SynRM motor design [3]. A persistent challenge in this domain is the selection of interpolation parameters that avoid numerical artifacts. Moreover, existing methods for handling relative motion between the stator and the rotor involve computationally expensive techniques such as remeshing, periodic boundary conditions [4] or sliding mesh [5], all of which complicate the adjoint sensitivity derivation due to the change in mesh topology.

This work advances the state of electric motor topology optimization via three key contributions. First, we present a general projection-based mapping framework that simultaneously handles rotor motion and density filtering within a static finite element mesh via a rotational transformation of design fields. While the projection techniques are widely used for density filtering in topology optimization, we demonstrate that the same formalism can effectively model the rotor motion by projecting a static rotor design onto a rotated mesh configuration without relying on mesh warping, sliding interfaces, or remeshing. This approach is mesh-agnostic, scalable, and applicable to any physical system where relative motion between domains must be captured, extending beyond electric motors. This projection also ensures a consistent design filtering across rotations, streamlining the computational workflow.

Second, we derive the exact adjoint sensitivities for both average torque and torque ripple, formulated as the ratio of RMS (Root Mean Square) torque to average torque over rotor positions, offering a performance-normalized consistent metric for ripple evaluation. Since there is no change in mesh topology during the rotation, the sensitivity formulation is simplified.

Additionally, we explore the role of interpolation factors on design exploration optimization convergence.

Finally, we integrate the method in a topology optimization of a high torque SynRM rotor design using a three-stage optimization strategy: an initial design with loose ripple constraint to maximize torque, followed by refinement under a tighter ripple constraint, and a final optimization with Heaviside projection to enhance discreteness in design while increasing torque without violating ripple bounds. This sequential tightening approach mitigates the optimization landscape's nonlinearity and facilitates convergence to high-performance, manufacturable designs.

II. ELECTROMAGNETIC FEA FORMULATION AND TORQUE EVALUATION

We model the electromagnetic behavior of the SynRM motor under the magnetostatic assumption. For the two-dimensional cross section of the machine, the variation of magnetic flux density $\underline{\mathbf{B}}$ is purely in xy plane, hence, the magnetic potential vector $\underline{\mathbf{A}}$ has only one non-zero component, $\underline{\mathbf{A}}_z$, perpendicular to the xy plane. The governing equation for $\underline{\mathbf{A}}_z$ then reduces to a scalar Piosson problems as:

$$\nabla \cdot (\nu \nabla \underline{\mathbf{A}}_z) = -\mathbf{J}_{\text{src}} \quad \text{in } \Omega, \tag{1a}$$

$$\mathbf{A}_{z} = 0 \quad \text{on } \Gamma \tag{1b}$$

where, J_{src} is the source term representing the current field density. The magnetic flux density ($\underline{\mathbf{B}}$) and magnetic field intensity vector ($\underline{\mathbf{H}}$) are computed as $\underline{\mathbf{B}} = \nabla \times \underline{\mathbf{A}}$ and $\underline{\mathbf{H}} = \nu \underline{\mathbf{B}}$ respectively, where ν represents the magnetic reluctivity. The Dirichlet boundary condition in (1) is imposed both on the stator outer surface and the inner rotor surface. We assume a constant reluctivity for ferromagnetic materials, adopting a linear magnetostatic formulation. While this simplification neglects magnetic saturation effects, it enables a focused assessment of the proposed rotated projection methodology and

its computational advantages in the topology optimization of rotating machines. The framework lays a scalable and extensible foundation for future integration of nonlinear magnetic material models.

The discrete linear two-dimensional finite-element formulation for (1) is given as

$$\mathbf{R} = \mathbf{K} \cdot \mathbf{A}_z - \mathbf{f} = \mathbf{0} \tag{2a}$$

where, $\underline{\mathbf{R}}$ is the global residual vector, $\underline{\mathbf{K}}$ is the global coefficient matrix, and $\underline{\mathbf{f}}$ is the global source vector. They are obtained by assembling element coefficient matrices $\underline{\mathbf{K}}_{a}$ and source vectors $\underline{\mathbf{f}}_e$ computed as follows:

$$\underline{\underline{\mathbf{K}}}_{e} = \int_{\Omega_{e}} \nu_{e} \underline{\nabla \mathbf{N}} \cdot \underline{\nabla \mathbf{N}} d\Omega_{e}$$
 (3a)

$$\underline{\mathbf{f}}_e = \int_{\Omega_e} \mathbf{J}_{\text{src}}^e \underline{\mathbf{N}} d\Omega_e \tag{3b}$$

where $\underline{\mathbf{N}}$ are the nodal shape functions and $\mathbf{J}^e_{\mathrm{src}}$ is the current density in each element. The reluctivity of each element, ν is related to the permeability, μ , as $\nu = \frac{1}{\mu}$. The permeability is taken to be one for non-ferrmagnetic (air and coils) and 5000 for ferromagnetic (iron) materials throughout.

The electromagnetic torque is evaluated using the Arrkio method [6], which is based on integration in the airgap region between the stator and the rotor. Assuming a circular airgap region of constant thickness centered at the origin, the electromagnetic torque can be expressed as the following volume integral over the airgap domain as

$$\tau = \frac{-L}{\mu_0 d} \int_{\Omega_{\text{airgap}}} \frac{\partial \underline{\mathbf{A}}_z}{\partial r} \frac{\partial \underline{\mathbf{A}}_z}{\partial \theta} d\Omega \qquad (4a)$$

where,
$$\begin{bmatrix} \frac{\partial \underline{\mathbf{A}}_{z}}{\partial \underline{R}_{z}} \\ \frac{\partial \underline{\underline{\mathbf{A}}}_{z}}{\partial \theta} \end{bmatrix} = \underline{\underline{R}}_{trans} \cdot \underline{\underline{\nabla}} \underline{\mathbf{N}} \cdot \underline{\mathbf{A}}_{z}$$
 (4b)

$$\underline{\underline{R}}_{\text{trans}} = \begin{bmatrix} \frac{x}{\sqrt{x^2 + y^2}} & \frac{y}{\sqrt{x^2 + y^2}} \\ -y & x \end{bmatrix}$$
 (4c)

Here, L is the motor axial length and d is the airgap thickness. The matrix $\underline{\underline{R}}_{trans}$ is a transformation matrix between the cartesian and polar coordinates evaluated at the $(x(\xi,\eta),y(\xi,\eta))$ locations, where (ξ, η) are the Gauss Quadrature coordinates used for numerical integration within each element.

III. PROPOSED DESIGN PROJECTION AND FILTERING

The proposed projection operator builds upon the classical density filtering in topology optimization. Density filtering mitigates mesh-dependency and checkerboard patterns by applying a spatial filter that maps design variables ρ to filtered physical densities as:

$$\tilde{\rho} = \underline{\underline{\mathcal{P}}} \cdot \underline{\rho} \tag{5a}$$

$$\hat{\mathcal{P}}_{i,j} = \left[\max\{1 - \frac{d_{i,j}}{r_0}, 0\} \right]^m$$
 (5b)

$$\mathcal{P}_{i,j} = \frac{\hat{\mathcal{P}}_{i,j}}{\sum_{i=1}^{n} \hat{\mathcal{P}}_{i,j}}$$
 (5c)

Here, r_0 is the characteristic length scale defining the filter's zone of influence, d_{ij} the Euclidean distance between element centroid i and j, and m = 3 controls the filter's strength. The resulting filter projection matrix $\underline{\mathcal{P}}$ offers a convenient and extensible technique to apply both rotation and density filtering to rotor designs. We modify the filtering procedure by computing d_{ij} between background centroids and rotated centroids at rotor angle $\theta = \theta_k$ using a rotation matrix $\underline{\mathcal{R}}_{\theta}$ as described below:

$$\underline{\underline{\mathcal{R}}}_{\theta} = \begin{bmatrix} \cos \theta & -\sin \theta \\ \sin \theta & \cos \theta \end{bmatrix} \tag{6a}$$

$$d_{i,j} = \|c_i^{\ 0} - \mathcal{R}_{\theta} c_i^0\|_2 \tag{6b}$$

where $c_i^{\ 0}$ is the centroid of the static background mesh. Consequently, the filtering and the rotor rotation are seamlessly managed simultaneously. Figure 1 demonstrates the rotation of initial rotor density field ρ to $\tilde{\rho}$ at various rotation angles using (5). The overall approach to obtain the projection matrix $\underline{\mathcal{P}}$ is shown in Algorithm 1.

Algorithm 1 Projection Matrix Assembly

```
1: procedure ASSEMBLEPROJECTIONMATRIX(\mathcal{M}, \theta, r_0, m)
             Input: Mesh \mathcal{M}, rotation angle \theta, search radius r_0,
      filter exponent m
             Output: Filter matrix \hat{P}
 3:
 4:
                                                          > Evaluate element centroids
             for i=1 to N_{\rm elem} do
 5:
                   Extract nodal coordinates of element i into C
 6:
                    c^0 \leftarrow column-wise mean of C
 7:
 8:
             end for
                                        \triangleright Rotate centroids (if \theta > 0) using (6)
 9:
             if \theta > 0 then
10:
                  \theta_{\text{rad}} \leftarrow \theta \cdot \pi / 180
\underline{\underline{\mathcal{R}}}_{\theta} \leftarrow \begin{bmatrix} \cos(\theta_{\text{rad}}) & -\sin(\theta_{\text{rad}}) \\ \sin(\theta_{\text{rad}}) & \cos(\theta_{\text{rad}}) \end{bmatrix}
for i = 1 to N_{\text{elem}} do
c^{\theta} \leftarrow \underline{\underline{\mathcal{R}}}_{\theta} \cdot c^{0}
11:
12:
13:
14:
15:
16:
             end if
              > Compute filter weights using pairwise search using
17:
      Alg. 2
             \mathcal{T} \leftarrow \text{NeighborhoodSearch}(c^0, c^{\theta}, r_0, m)
18:
                                   \triangleright Assemble sparse matrix \mathcal{P} from triplets
19:
             \mathcal{P}(i,j) \leftarrow \text{assembled from triplets in } \mathcal{T}
20:
                                                \triangleright Normalize rows of \mathcal{P} using (5c)
21:
```

for k=1 to number of rows in $\hat{\mathcal{P}}$ do

 $\hat{\mathcal{P}}_{kj} \leftarrow \mathcal{P}_{kj}/s_k$

for all nonzeros \mathcal{P}_{ki} in row k do

 $s_k \leftarrow \sum_j \mathcal{P}_{kj}$ if $s_k \neq 0$ then

end for

end if end for

29: 30: end procedure

22:

23:

24:

25:

26:

27:

28:

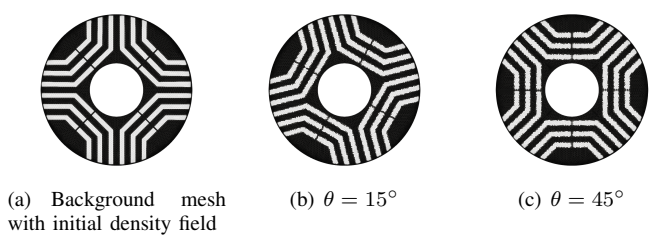


Fig. 1: Rotor design projection onto fixed background mesh at various rotor orientation.

In the proposed method, the projected physical density of an element is computed as a weighted average of the densities of all rotated mesh centroids lying within its zone of influence. The brute-force implementation, detailed in Algorithm 2, performs an exhaustive $\mathcal{O}(n^2)$ pairwise distance check between each background and rotated centroid, storing the indices and corresponding weights for all neighbors within the specified radius. While straightforward, this approach incurs a significant computational cost as the mesh resolution increases. To address this bottleneck, we adopt the TreeNSearch algorithm, which leverages an octree-based spatial indexing structure to accelerate neighborhood queries [7]. TreeNSearch constructs a two-level acceleration structure that clusters non-empty partitions and adaptively traverses the domain, enabling efficient sparse projection matrix assembly even for large-scale, highresolution meshes. A detailed performance comparison with the brute-force approach is provided in Section V.

Algorithm 2 Brute Force Neighborhood Search

```
1: procedure NeighborhoodSearch(c^0, c^\theta, r_0, m)
         Input: Centroids c^0 (before rotation), c^{\theta} (after rota-
    tion), search radius r_0, filter exponent m
         Output: Triplet list \mathcal{T} (row, column, weight)
3:
                   ▷ Initialize triplet list and nonzero count array
4:
         \mathcal{T} \leftarrow \text{empty list}
5:
         nnzs \leftarrow zeros(N_{elem})
6:
7:
            > Perform pairwise search between centroids using
    (5b)
         for i=1 to N_{\text{elem}} do
8:
             for j=1 to N_{\text{elem}} do
9:
                  d_{ij} \leftarrow \|c_i - c_j\|/r_0
10:
                  w_{ij} \leftarrow \max(0, 1 - d_{ij})^m
11:
12:
                  if w_{ij} > \varepsilon then
                       Append (i, j, w_{ij}) to \mathcal{T}
13:
                       nnzs(i) \leftarrow nnzs(i) + 1
14:
                  end if
15:
             end for
16:
17:
         end for
18:
         return \mathcal{T}
19: end procedure
```

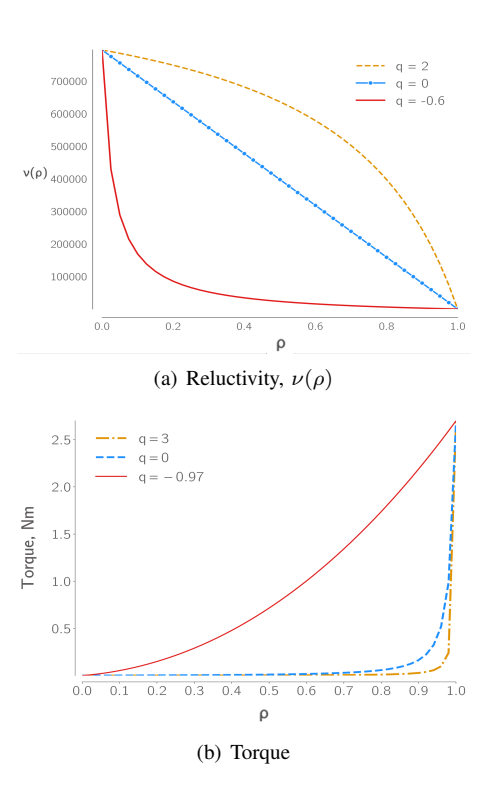


Fig. 2: Effect of RAMP interpolation on intermediate design variables. The entire rotor domain is assigned an intermediate value ρ .

IV. TOPOLOGY OPTIMIZATION FRAMEWORK

We use a density-based approach to parameterize the rotor design space. In this method, each finite element in the rotor design domain is assigned a design variable, called the material density, $\rho \in [0,1]$. We use the Rational Approximation of Material Properties (RAMP) scheme to interpolate the material's reluctivity between air (ν_0) and ferromagnetic material (ν_m) as follows:

$$\nu = \nu_m \left[\frac{\tilde{\rho}}{1 + q(1 - \tilde{\rho})} \right] + \nu_0 \left[1 - \frac{\tilde{\rho}}{1 + q(1 - \tilde{\rho})} \right]$$
 (7)

where q is an interpolation parameter [8] and $\tilde{\rho}$ is the density after the filtering projection is applied. Figure 2 shows the effect of RAMP interpolation on intermediate densities. The rotor is initialized with a constant density between 0 and 1, and the torque is evaluated for different interpolation parameters q. For $q \geq 0$, most intermediate densities yield similar torque response, causing the premature optimization termination. To improve the design space exploration, we use $q \in (-1,0)$, where the effective reluctivity and torque exhibit a concave profile, facilitating smoother convergence in gradient-based optimization. In our work, we use q = -0.7.

We seek an SynRM rotor topology that maximizes the average torque produced at various rotor angles while constraining the mass of the rotor and the torque ripple. The topology

optimization formulation is shown as follows:

$$\begin{aligned} & \underset{\rho_{e}}{\text{max}} & T_{avg} \\ & \text{s.t.} & T_{ripple} \leq T_{ripple}^{*} \\ & \sum_{i=1}^{n_{e}} \frac{\rho_{i}v_{i}}{V_{max}} \leq v_{f} \\ & \underline{\mathbf{K}}\underline{\mathbf{A}}_{z} = \underline{\mathbf{f}} & \forall \quad \theta = 0^{\circ}, 15^{\circ}, \dots \\ & 0 < \rho_{e_{min}} \leq \rho_{e} \leq 1 \end{aligned} \tag{8}$$

where T_{avg} is the average torque. The torque at each angle is evaluated using the rotated filtering technique proposed in this work. The torque ripple factor, T_{ripple} , is defined as the ratio of the RMS (T_{rms}) to the average torque magnitude, with T_{ripple} constrained to be below T_{ripple}^* . Since the average torque changes over iterations, this normalized ratio offers a consistent comparison. The torque ripple and average torque are computed as:

$$\tau_{\text{avg}} = \frac{1}{n} \sum_{r=1}^{n} \tau(\theta_r) \tag{9a}$$

$$\tau_{\rm rms} = \sqrt{\frac{1}{n} \sum_{r=1}^{n} \tau^2(\theta_r)} \tag{9b}$$

$$\tau_{\text{ripple}} = \frac{\tau_{\text{rms}}}{|\tau_{\text{avg}}|} \tag{9c}$$

Additionally, a mass fraction constraint of v_f is applied for a lightweight design. In (8), v_i is the volume of each finite element in the rotor domain and $V_{max} = \sum_{i}^{n_e} v_i$ is the total volume of the rotor design domain with $\rho = 1$.

A. Adjoint-based Sensitivity Analysis

The derivative of individual torque τ with respect to design variables ρ is derived using the discrete adjoint sensitivity analysis approach. First, the gradients with respect to the filtered densities are obtained as

$$\frac{d\tau}{d\tilde{\rho}} = \frac{\partial \tau}{\partial \tilde{\rho}} + \underline{\psi} \cdot \frac{\partial \mathbf{R}}{\partial \tilde{\rho}}$$
 (10a)

$$\frac{\partial \mathbf{R}}{\partial \tilde{\rho}} = \prod_{e=1}^{nelem} \frac{\partial \nu}{\partial \tilde{\rho_e}} \underline{\mathbf{K}}_e^0$$
 (10b)

where $\underline{\mathbf{K}}^0$ is the element coefficient matrix with $\nu = 1$. The operator \prod_{e} represents the additive assembly of individual element contribution to global matrix. The corresponding adjoint vector ψ can be obtained by solving

$$\underline{\underline{\mathbf{K}}\psi} = -\frac{\partial \tau}{\partial \underline{\mathbf{A}}_z} \tag{11}$$

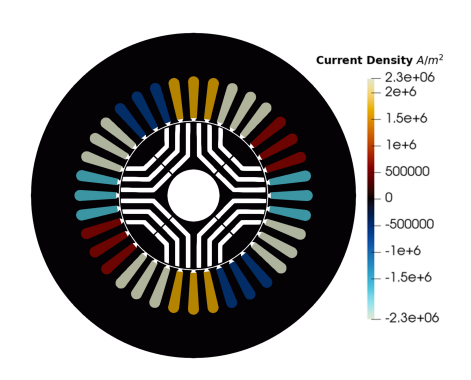


Fig. 3: Benchmark SynRM model with two-pole pairs and 36 slots. The stator and rotor ferromagnetic material is shown in black. The current densities in the coils are shown as well.

For the torque at a given angle θ corresponding to projected densities $\tilde{\rho}$,

$$\frac{\partial \tau}{\partial \tilde{\rho}} = \underline{0} \tag{12a}$$

(9a)
$$\frac{\partial \tau}{\partial \underline{\tilde{\rho}}} = \underline{0}$$

$$\frac{\partial \tau}{\partial \underline{\mathbf{A}}_{z}} = -\frac{L}{\mu_{0}d} \int_{\Omega_{\text{gap}}} \left[\frac{\partial}{\partial \underline{\mathbf{A}}_{z}} \frac{\partial \underline{\mathbf{A}}_{z}}{\partial r} \cdot \frac{\partial \underline{\mathbf{A}}_{z}}{\partial \theta} + \frac{\partial \underline{\mathbf{A}}_{z}}{\partial r} \cdot \frac{\partial}{\underline{\mathbf{A}}_{z}} \frac{\partial \underline{\mathbf{A}}_{z}}{\partial \theta} \right] d\Omega$$

$$(9c) \quad \frac{\partial}{\partial \underline{\mathbf{A}}_{z}} \begin{bmatrix} \frac{\partial \underline{\mathbf{A}}_{z}}{\partial T} \\ \frac{\partial \underline{\mathbf{A}}_{z}}{\partial \theta} \end{bmatrix} = \underline{\underline{R}}_{trans} \cdot \underline{\nabla} \underline{\mathbf{N}}$$
(12c)

Here, $\underline{\underline{R}}_{trans}$ is the transformation matrix used in the torque computation in (4). Since the projection matrix $\underline{\mathcal{P}}$ has the dual purpose of rotor rotation as well as design filtering to prevent the checkerboard pattern, the total derivative of torque at a specific rotor angle with respect to the design variables is

$$\frac{d\tau}{d\underline{\rho}} = \underline{\underline{\mathcal{P}}}^T \cdot \frac{d\tau}{d\underline{\tilde{\rho}}} \tag{13}$$

After evaluating the sensitivity of torque at each angle, we apply chain rule differentiation in (9) to obtain

$$\frac{d\tau_{avg}}{d\underline{\rho}} = \frac{1}{n} \sum_{r=1}^{n} \frac{d\tau(\theta_r)}{d\underline{\rho}}$$
 (14a)

$$\frac{d\tau_{rms}}{d\underline{\rho}} = \frac{1}{n\tau_{rms}} \sum_{r=1}^{n} \left[\tau(\theta_r) \frac{d\tau(\theta_r)}{d\underline{\rho}} \right]$$
(14b)

$$\frac{d\tau_{ripple}}{d\underline{\rho}} = \frac{\tau_{avg} \frac{d\tau_{rms}}{d\underline{\rho}} - \tau_{rms} \frac{d\tau_{avg}}{d\underline{\rho}}}{(\tau_{avg})^2}$$
(14c)

V. RESULT

In this section, we demonstrate the proposed motor topology optimization framework using rotated projection filtering approach for a representative SynRM design shown in Fig. 3. The motor is a three-phase, two pole-pair type with an axial length of 0.135 m, an air gap width of 0.0025 m, 36 slots, and 18 turns per winding. The peak rated current is 28.284 A per turn with a phase angle of 45°.

TABLE I: Torque prediction error percentage relative to COM-SOL prediction for various mesh refinement

Mesh	Number of Elements	Torque (N m)	%Error
Coarse	69.188	5.4916	7.95
Medium	130,796	5.1359	0.96
Fine	227,338	5.13241	0.89
Finest	268,050	5.1294	0.83

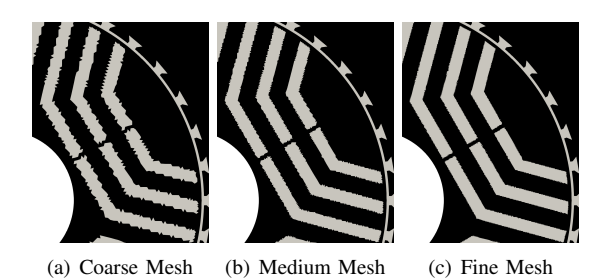


Fig. 4: Effect of mesh resolution on projected rotor geometry at $\theta=85^{\circ}$. Coarser meshes lead to jagged edges and loss of detail in rotor, while finer meshes preserve the original geometry accurately. Sufficient refinement is essential to maintain fidelity, especially near air-slot boundaries.

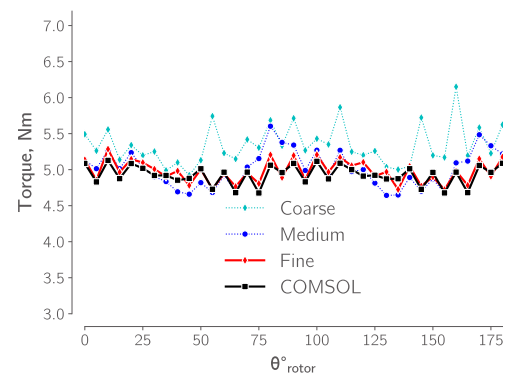
A. Model Validation

The SynRM motor layout in Fig. 3 is analyzed using the developed finite element framework as well as COMSOL software at 0° rotor orientation as shown in Fig. 1. For the given setup, the geometry is discretized using 227, 338 triangle isoparametric elements and analyzed in COMSOL to obtain the standard electromagnetic torque as 5.0867 N m. The geometry is then analyzed with different mesh sizes using the developed framework. The grid convergence results with percentage error with respect to COMSOL torque are shown in Table I . A coarse mesh results is significant discretization error. The medium mesh with approximately twice the element count results in accurate torque calculation within 1% error margin. Further refinement does not improve the torque prediction significantly, indicating grid convergence.

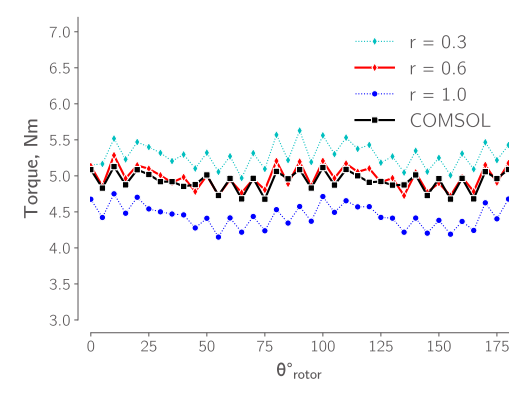
1) Impact of Mesh Resolution

To assess the impact of mesh resolution on the quality of projected rotor geometry, we visualize the projected design at $\theta=85^\circ$ using coarse, medium, and fine background meshes as shown in Fig. 4. The coarse mesh fails to preserve the rotor edges, introducing geometric artifacts that degrade the torque accuracy. In contrast, the mesh refinement significantly improves projection accuracy, particularly along the edges.

Figure 5(a) compares the torques predicted by the proposed method at rotor angles from 0° and 180° in 15° increments for different mesh resolutions. While both medium and fine meshes show good agreement with reference COMSOL torque at $\theta=0^{\circ}$, only the fine mesh maintains the consistent accuracy across all angles, highlighting the importance of sufficient spatial resolution for reliable torque evaluation throughout the rotor's motion. High-resolution meshes are also desirable from a topology optimization standpoint, as they enable finer structural features and more accurate gradient information.



(a) Effect of mesh resolution: Finer meshes better resolve the projected rotor geometry, resulting in closer agreement with the COMSOL reference solution.



(b) Effect of projection radius: A smaller projection radius omits geometric details, while an excessively large radius introduces fictitious features, both leading to inaccurate torque estimation

Fig. 5: Comparison of torque predicted using the projection approach with COMSOL at various rotor angles.

2) Impact of Projection Radius r_0

We analyzed the influence of projection radius on the geometric fidelity of the projected design. Increasing the projection radius causes the projected densities to be averaged over a broader neighborhood and thus blurs the material boundary. This smoothing effect tends to lower the predicted torque, as illustrated in Figure 5(b). Conversely, an excessively small projection radius can introduce artificial air gaps and holes during rotation due to the generally irregular mesh points. These gaps lead to inflated torque predictions and thus reduce accuracy. Through parametric studies, we found that selecting a projection radius within the range $r_0 \in [2\Delta s, 6\Delta s]$, where Δs is the background mesh edge length, strikes an effective balance between preserving the geometric fidelity and maintaining sharp edges. Additionally, maintaining the number of nonzero component per row in the projection matrix $\underline{\mathcal{P}}$ between 10 and 30 was empirically determined to be optimal for preserving geometric details without excessive smoothing.

3) Computational Efficiency

To address concerns regarding the computational cost of pairwise neighborhood searches, we benchmarked the performance of a brute-force implementation against an octreeaccelerated approach using the TreeNSearch library. As shown

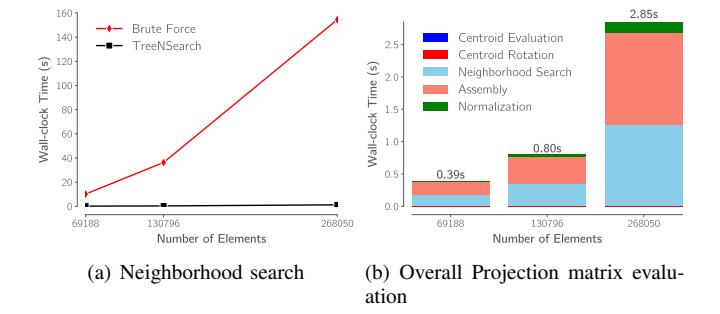


Fig. 6: Comparison of projection matrix assembly performance across three mesh resolutions. (a) Wall-clock time for neighborhood search using brute-force and TreeNSearch methods, highlighting the scalability and efficiency of the latter. (b) Breakdown of wall-clock times for individual steps in the TreeNSearch-based projection matrix computation.

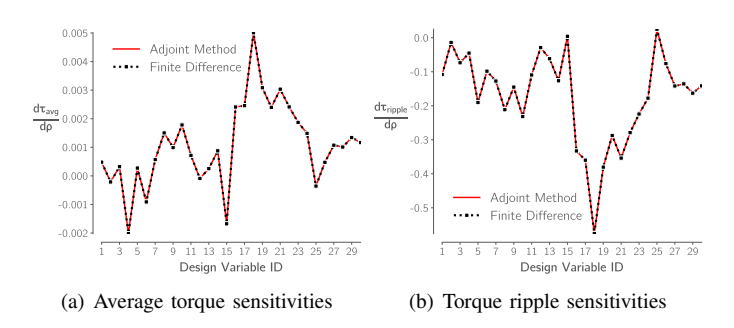
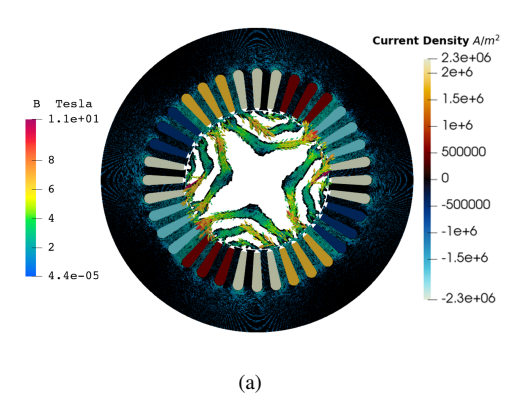


Fig. 7: Comparison of adjoint sensitivities with central finite difference scheme with $\Delta h=1e-8$ for randomly assigned design variables

in Fig. 6, the brute-force method exhibits quadratic growth in runtime with increasing mesh size, making it impractical for high-resolution problems. In contrast, TreeNSearch scales nearly linearly due to its spatial partitioning strategy, yielding over two orders of magnitude speedup on the largest mesh tested. Both methods identify identical neighbor sets, and the matrix normalization step, common to both pipelines, was excluded from timing to isolate the performance of the neighborhood search itself. While the growth of pairwise computations is inevitable in high-dimensional problems, TreeNSearch ensures that the assembly of the projection matrix remains efficient, even as the mesh size increases. This efficiency is especially crucial when performing large-scale topology optimizations, where computational cost becomes a critical factor.

B. Sensitivity Validation

We validate our analytical derivations of the sensitivities for the torque-based objective and constraint functions by comparing them with those obtained from central difference with a step size of $\Delta h=1\times 10^{-8}$. The rotor design domain in the SynRM geometry is initialized with random design variables between 0 and 1, and torques are evaluated at 12 rotor angles between 0° and 180° at 15° intervals.



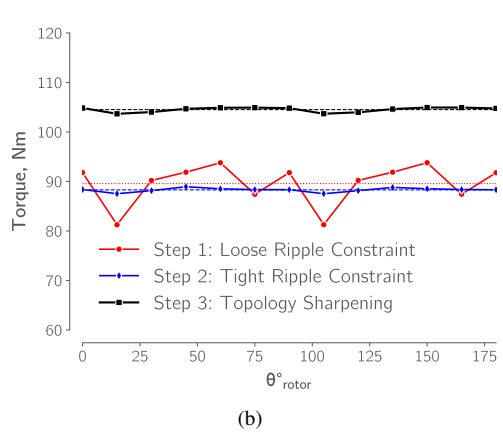


Fig. 8: Topology optimization result for SynRM rotor with a multistage approach: (a) SynRM design with final converged optimal rotor. (b) Torque profile with optimal rotors after each stage.

Figure 7 shows excellent agreement between analytical and numerical derivatives with respect to first 30 design variables. The sensitivities of the volume constraint is straightforward and available in the literature, hence, we do not include them for the sake of conciseness.

C. Topology Optimization

We apply the technique developed to optimize the rotor layout for the SynRM motor shown in Fig. 3 with constraints on maximum volume fraction at 65% and torque ripple factor at 1.00001. The rotor design variables are initialized uniformly at 0.9. The final rotor material distribution shown in Fig. 8(a) constitutes a distinct periodic pattern with air barriers to guide the magnetic fields. To handle the numerical difficulties associated with the nonlinear objectives and constraints, we solve the problem in a multi-stage approach as follows:

• Step 1 with Loose Ripple Constraint: A relaxed ripple constraint of 1.001 is set, allowing the optimizer to achieve a feasible design rapidly with $\tau_{avg}=89.5~\mathrm{N}\,\mathrm{m}$, rotor volume fraction of 0.48, and $\tau_{ripple}=1.001$. This corresponds to a maximum torque deviation of 9% from average torque due to local fluctuations in torque. Most of the design exploration is performed in this stage. Figure 9

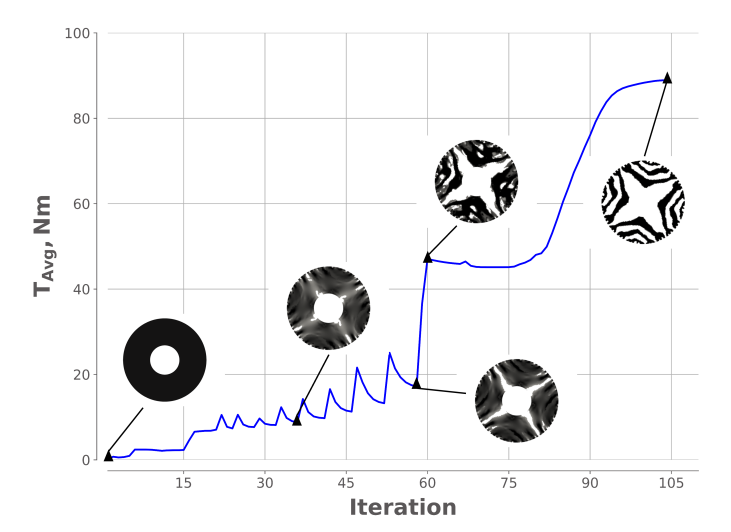


Fig. 9: Rotor design evolution along with maximization of average torque during optimization convergence in Step 1.

shows the rotor design evolution through iterations until convergence in Step 1.

- Step 2 with Tight Ripple Constraint: The optimal design from step 1 is used as initial point for another optimization with a tighter ripple constraint of 1.00001 to smoothen out the torque fluctuations via localized adjustments. The maximum torque deviation is reduced to <1% of average torque. This results in slight decrease in τ_{avg} and volume fraction to $88~\mathrm{N\,m}$ and 0.47 respectively.
- Step 3 with Topology Sharpening: Finally, the optimal design from step 2 is used as initial point for a third optimization problem, wherein, a Heaviside step projection filter is incorporated, with the sharpness gradually increased from 1 to 16. This allows to obtain a discrete design without any intermediate densities. As a result, we obtain an optimal design with $\tau_{avg}=104.5~\mathrm{N}~\mathrm{m}$, volume fraction of 0.466, and a low $\tau_{ripple}=1.00001$. The improvement in torque profile in final step is shown in Fig. 8(b).

VI. CONCLUDING REMARKS

In this work, we present a unified framework for topology optimization of electric motors, which simplifies the rotor rotation handling through a modified density filtering on a static background mesh, eliminating the need for remeshing or sliding mesh methods. The accuracy and computational cost of this technique are carefully examined by varying various factors such as grid size and projection radius. Finally, we apply the method to optimize a SynRM rotor to achieve a lightweight design with a maximum average torque and low torque ripple. The RAMP interpolation with suitable profiles improves design space exploration. Future work will extend this approach to include multiphysics constraints and material non-linearities.

REFERENCES

- [1] C. Lee and I. G. Jang, "Topology optimization of multiple-barrier synchronous reluctance motors with initial random hollow circles," *Structural and Multidisciplinary Optimization*, vol. 64, pp. 2213–2224, 2021.
- [2] C. Lee, J. Lee, and İ. G. Jang, "Topology optimization for the manufacturable and structurally safe synchronous reluctance motors with multiple iron webs and bridges," *IEEE Transactions on Industrial Electronics*, vol. 70, no. 1, pp. 678–687, 2022.
- [3] M. Garibaldi, C. Gerada, I. Ashcroft, and R. Hague, "Free-form design of electrical machine rotor cores for production using additive manufacturing," *Journal of Mechanical Design*, vol. 141, no. 7, p. 071401, 2019.
- [4] M. Jabbar, H. N. Phyu, Z. Liu, and C. Bi, "Modeling and numerical simulation of a brushless permanent-magnet dc motor in dynamic conditions by time-stepping technique," *IEEE Transactions on industry applications*, vol. 40, no. 3, pp. 763–770, 2004.
- vol. 40, no. 3, pp. 763–770, 2004.
 [5] D. Meeker, "Sliding band motion model for electric machines," *Finite Element Method Magnetics*, 2018.
- [6] A. Arkkio et al., Analysis of induction motors based on the numerical solution of the magnetic field and circuit equations. Helsinki University of Technology, 1987.
- [7] J. A. Fernández-Fernández, L. Westhofen, F. Löschner, S. R. Jeske, A. Longva, and J. Bender, "Fast octree neighborhood search for sph simulations," *ACM Transactions on Graphics (TOG)*, vol. 41, no. 6, pp. 1–13, 2022.
- [8] M. Stolpe and K. Svanberg, "An alternative interpolation scheme for minimum compliance topology optimization," *Structural and Multidisciplinary Optimization*, vol. 22, pp. 116–124, 2001.